THE JOURNAL OF PHYSICAL CHEMISTRY C
A JOURNAL OF THE AMERICAN CHEMICAL SOCIETY

pubs.acs.org/JPCC

Article

Bubble-Printed Microscale Silver Thermistors

Published as part of The Journal of Physical Chemistry C virtual special issue "Photothermal and Non-Fluorescent Imaging in Microscopy and Spectroscopy."

Anand Swain, Pavana Siddhartha Kollipara, and Yuebing Zheng*

Cite This: *J. Phys. Chem. C* 2024, 128, 7316–7322

Read Online

ACCESS | Metrics & More | Article Recommendations | Supporting Information

ABSTRACT: Microscale temperature sensing and control are essential in various applications. Thermistors are widely utilized for temperature sensing owing to their simple design and high sensitivity. The future of thermistors lies in miniaturization and integration in highly customizable and sustainable electronics. Moreover, the ever-reducing size of the transistors requires the thermistors to scale down proportionally, without any compromise to its functionality. However, fabricating microscale thermistors exhibiting high accuracy and repeatable measurements has been challenging for state-of-the-art device miniaturization. Here, we develop versatile printing of microscale thermistors from silver fluoride solution by exploiting laser-induced opto-thermal microbubbles. The microscale temperature gradients on the bubble surface create an enhanced concentration of silver ions around the bubble to enable high-resolution printing of submicrometer structures with low-concentration precursors and low wastage. We demonstrate the bubble printing of thermistor arrays with both positive and negative thermal coefficients by exploiting the size effect on the electrical conductivity. We further investigate the sensing performance and long-term stability of the printed thermistors and conclude that the bubble-printed thermistors exhibit high-resolution sensing capabilities with long-term stability, promising enhanced performance in medical and semiconductor applications.

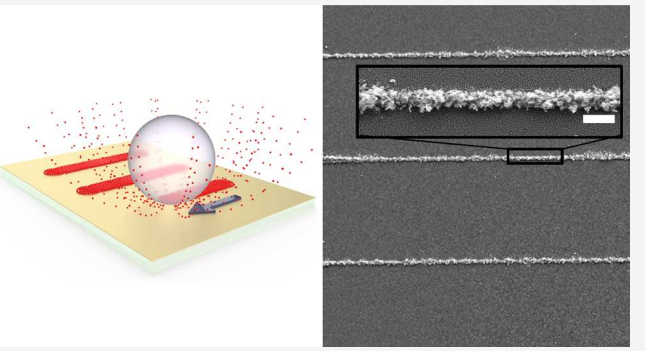

1. INTRODUCTION

Temperature control at the microscale plays a vital role across various domains, including biology,[1,2] agriculture,[3] energy storage,[4] and microflow environments, where accurate microscale sensing is crucial to monitor these changes.[5−7] Commonly employed methods include thermistors,[8,9] microthermocouples,[10,11] and optical interferometry.[12,13] Thermistors are popular in microscale temperature-sensing applications as their small size, simple design, and rapid response time make them ideal candidates for integration in a wide array of applications where precise and localized measurements are needed, especially in the semiconductor industry.[14,15] Thermistors are traditionally categorized as either PTC (positive thermal coefficient) or NTC (negative thermal coefficient) based on the change in resistivity with temperature change. PTC thermistors are typically composed of conductive metals or doped ceramics, while NTC thermistors are based on transition metal oxide ceramics that exhibit semiconducting behavior.[16] State-of-the-art thermistors are fabricated from barium titanate ($BaTiO_3$), which demonstrates PTC behavior or NTC behavior depending on the nature and concentration of the dopants.[17] However, multiple challenges arise from size effects that inhibit miniaturization of $BaTiO_3$ thermistors, including compositional inhomogeneity and reduced operational lifetimes.[18] In addition, issues such as contact resistance, inhomogeneous heating,[19−21] and delamination fracture[21,22] arise in practical device applications, rendering $BaTiO_3$ unsuitable for further thermistor miniaturization.

One approach to counter this has been the development of metallic thermistors. However, metals typically exhibit only PTC behavior, with careful surface modifications required to fabricate NTC thermistors.[23] Fortunately, the size effect on the electrical conductivity of metals offers a potential solution. Factors such as grain boundary scattering can significantly influence electrical conductivity of metals and become relevant at the micro and nanoscale.[24−26]

Direct writing techniques using nanoparticle inks can achieve versatile conduction behavior as they offer highly customizable microstructures of the printed materials. Such

Received: January 28, 2024
Revised: April 6, 2024
Accepted: April 8, 2024
Published: April 19, 2024

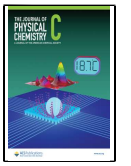

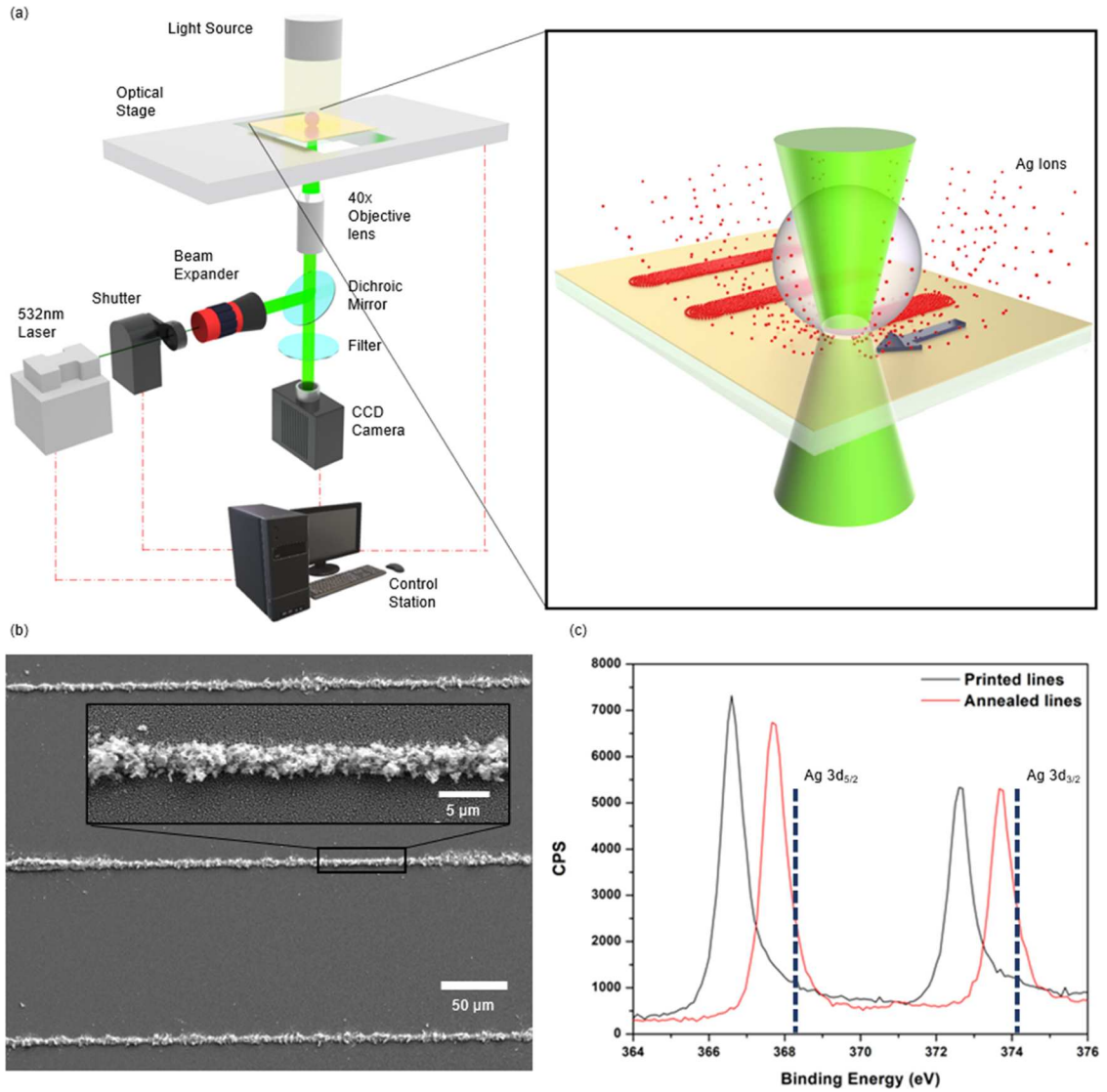

Figure 1. Overview of the thermistor fabrication process. (a) Schematic of the optical setup. The laser source, electronic shutter, and microscope stage are connected to a control station to enable centrally controlled patterning. A charge couple device (CCD) camera is also connected to the control station for visual observation. A close-up of the microbubble is depicted on the right. (b) SEM images of the printed lines, with an inset zoomed-in image. (c) XPS analysis shows that the annealing causes a shift in the 3d peaks of the printed patterns from AgO toward Ag.

methods are economical,[27] low-waste,[28] and user-friendly[29] alternatives to conventional lithography. In particular, on-demand fabrication capabilities of direct-write technologies are ideal for prototyping devices across various fields[30] as sensor systems[31,32] and diagnostic tools.[33,34] Among the direct writing approaches, ink/nozzle-based printing techniques (i.e., inkjet and E-Jet)[35,36] have gained recognition for high-precision, mask-free, and low-waste substance deposition on substrates. However, they are unable to manufacture complex structures at submicron resolution due to ink spreading,[37] the coffee-ring effect,[38] lengthy postprocessing times,[39] and hydrodynamically complex precursors, which can restrict the choices of printable moieties.[40] Although significant progress has been achieved in the direct writing of microscale thermistors over the past two decades, additional miniaturization is imperative to elicit size effects and attain versatile thermistor functionality.[41−44]

In this work, we seek to overcome these challenges through bubble-pen lithography (BPL) or bubble printing of versatile submicron silver thermistors. BPL has emerged as a printing technique that addresses several current challenges of the direct writing techniques.[45−48] BPL leverages Marangoni convection to drive ions, molecules, and colloidal nanoparticles to the solid−liquid interface of laser-induced opto-thermal microbubbles to print a wide range of moieties onto substrates.[46,49−51] BPL facilitates nanoparticle patterning with controllable deposition profiles, which we exploit to fabricate versatile silver thermitors for temperature sensing. By generating and translating opto-thermal microbubbles, we pattern microscale silver thermistors at high throughput, high resolution, and low wastage using economical, low-concentration (0.05 M) silver fluoride (AgF) solution of low volumes (15 μL). Through parametric studies, we have achieved the printing of both PTC and NTC thermistor arrays by exploiting the size-dependent electrical conductivity of silver microstructures. The long-term stability of the printed thermistors is high, revealing the strong viability of the thermistors in various applications.[52]

https://doi.org/10.1021/acs.jpcc.4c00598
J. Phys. Chem. C 2024, 128, 7316−7322

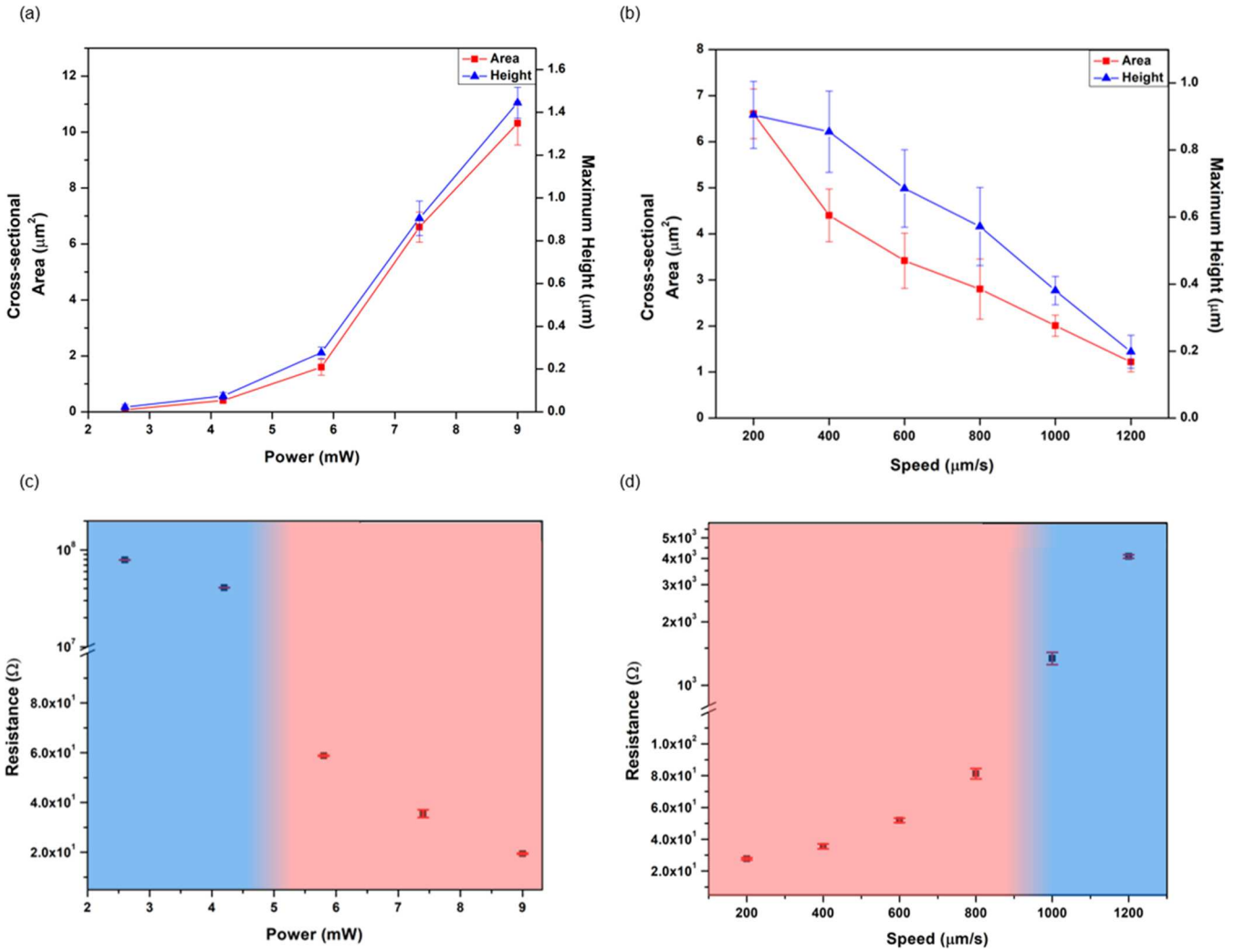

Figure 2. Height and cross-sectional profiles of printed lines with corresponding thermistor characteristics. (a) Cross-sectional height and area profiles with variation in laser power from 2.6 to 9 mW. (b) Variation of cross-sectional height and area of the printed lines as a function of printing speed from 200 μm/s to 1200 μm/s. (c) The electrical resistance at 296 K in the printed lines decreases as the printing power is increased, with a sharp change between 4.2 and 5.8 mW of laser power. (d) The resistance increases when the printing speed is increased, with a sharp increase beyond 800 μm/s.

2. EXPERIMENTAL METHODS

2.1. Fabrication of Silver Thermistors. *2.1.1. Substrate and Precursor Preparation.* Gold nanoislands (AuNI) were fabricated on borosilicate glass coverslips by deposition and subsequent annealing. A 4.5 nm Au thin film was deposited using thermal deposition (Nano 36 thin film deposition system, Kurt J Leskar Company), followed by thermal annealing at 823 K for 2 h. The precursor solution was prepared by using AgF salt (Fisher Scientific) dissolved in DI water at a concentration of 0.05 M.

2.1.2. Optical Setup for Bubble Printing. A schematic of the optical setup is depicted in Figure 1a. The stage, shutter, laser, and camera are centrally controlled from a control station. As shown in the inset, the laser-generated heat on the AuNI leads to bubble formation, and the resulting Marangoni convection leads to accumulation-driven printing of Ag. The relative motion of the laser spot with the translation of the optical stage leads to controlled Ag patterning. Further, a shutter is employed to introduce breaks in the printed pattern, allowing for discontinuous printing patterns. Three parallel Ag lines (300 μm in length) were printed in a single array.

2.1.3. Annealing. After deposition, the Ag lines were annealed in a vacuum oven (Isotemp Vacuum Oven, Model 281A, Fisher Scientific) at 453 K for 2 h. Scanning electron microscopy (SEM) images (obtained on FEI Quanta 650 ESEM) of the printed Ag lines post annealing are shown in Figure 1b, with a zoomed-in image inset. The effects of annealing were observed through X-ray photoelectron spectroscopy (obtained on a PHI VersaProbe4 XPS), as depicted in Figure 1c. Annealing converted some of the printed silver oxide (AgO) lines to pure Ag, improving the electrical conductivity.

2.2. Electrical Characterization. Ag electrodes (1 μm thickness) were deposited by thermal evaporation (Nano 36 thin film deposition system, Kurt J Lesker Company) to electrically characterize the printed thermistors. Optical fibers (250 μm diameter) were taped across the Ag lines as a shadow mask. Post deposition, the samples were coated in a polymer layer (SU-8 epoxy) to protect the samples from corrosion in air and to provide long-term stability. Characterization of the samples was carried out using a sourcemeter (Keithley 2612B) on a hot plate (Fisher Scientific Isotemp 11-100-49SH). The

https://doi.org/10.1021/acs.jpcc.4c00598
J. Phys. Chem. C 2024, 128, 7316−7322

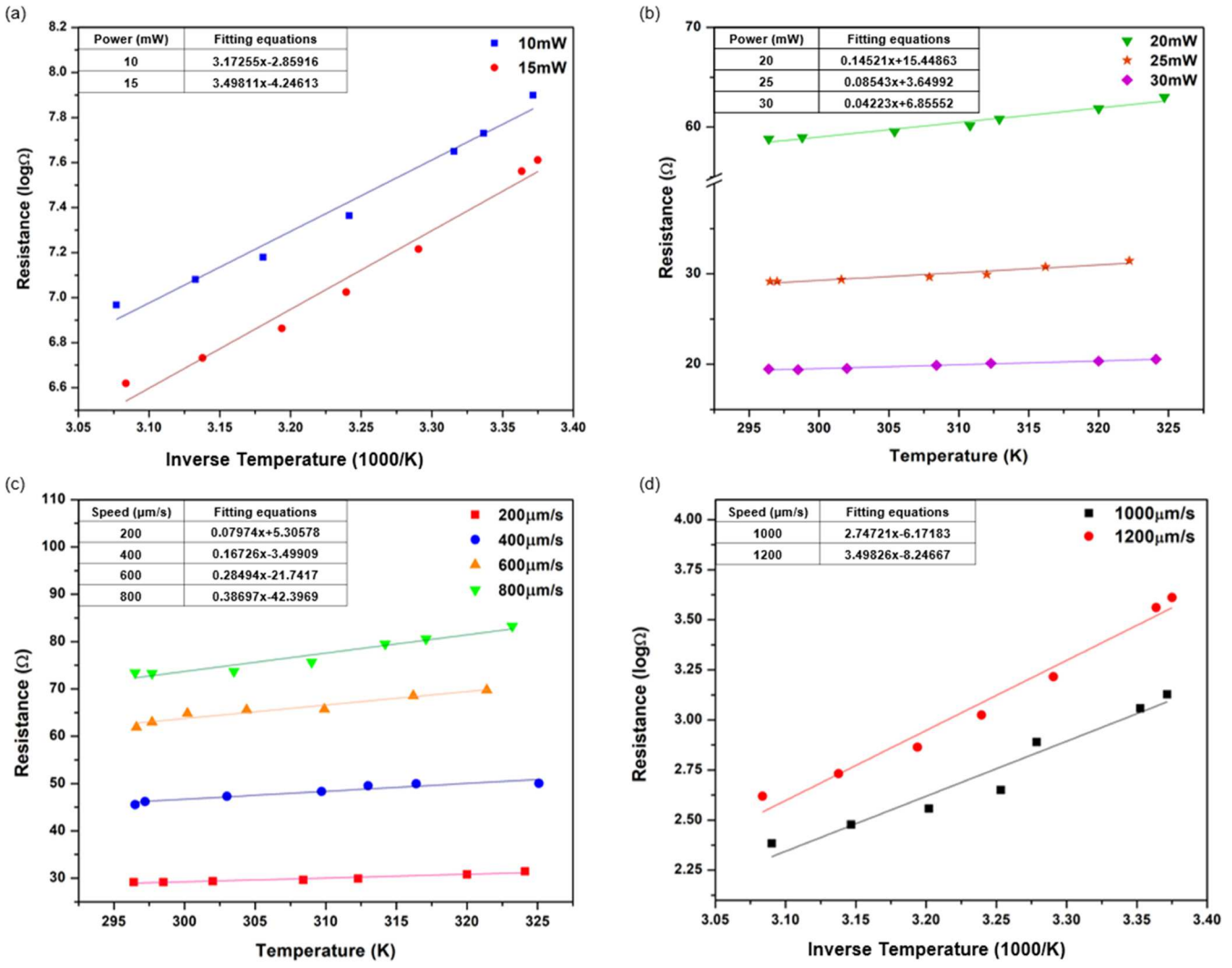

Figure 3. Change in electrical resistance with temperature for NTC and PTC thermistors, with respective fitting equations. (a) Printed NTC thermistors show an associated linear increase in the logarithmic resistance, when plotted against the adjusted inverse of the absolute temperature. (b) Printed PTC thermistors show a linear increase in resistance with temperature, with higher laser power being associated with more conductive behavior. (c) With 7.4 mW printing power, higher resistance occurs at the higher printing speeds, with a linear dependence of resistance on the temperature. (d) Thermistors printed at 1000 and 1200 μm/s display NTC.

temperature measured from a contact thermometer (Amprobe TPP2-C1) was used to measure the exact surface temperature and correlate this with the measured resistance. Resistance measurements were carried out in the range of 296−325 K. The performance of our printed thermistor was evaluated against a hand-held infrared thermometer (Nubee NUB8580) in determining the temperature of a gravity convection oven (Fisher Scientific Isotemp Oven Model: 6905). Measurements were carried out at 4 temperatures and averaged over multiple measurement areas to account for hotspots.

3. RESULTS AND DISCUSSION

3.1. Room-Temperature Characteristics. We first evaluated the effect of the laser power on the patterning of thermistors at a printing speed of 200 μm/s with 2.6 mW (1.6 mW/μm^2 optical intensity) being the minimum power needed for bubble formation in the AgF solution. We observed a sharp increase in the average height of the printed lines upon increasing the power from 4.2 to 5.8 mW, while there is a more gradual change in average cross-sectional areas of the lines. The cross-sectional areas and deposited heights of the printed lines are influenced by the morphology of the bubbles generated during the printing process. Higher laser power promotes the formation of larger bubbles with increased contact area on the substrate. The observed increase in material deposition, particularly with larger and stable bubbles, can be attributed to their extended contact duration with the substrate, as indicated by the higher heights of the lines. We employed optical profilometry to measure the cross-sectional areas and maximum heights of the printed lines as a function of laser power, as presented in Figure 2a.

Further, we studied the effects of the printing speed on the resultant patterns. The printing speed varied from 200 to 1200 μm/s with a laser power of 7.4 mW. We observed a gradual decrease in the areas and maximum heights of the printed lines with an increase in the printing speed. Optical profilometry results for variations in printing speed are presented in Figure 2b. When the printing speed is increased, it leads to a decrease in the duration of the bubbles and their contact areas with the substrate. As a result, the heights of the deposited lines decrease and the widths of the printed lines become narrower.

https://doi.org/10.1021/acs.jpcc.4c00598
J. Phys. Chem. C 2024, 128, 7316−7322

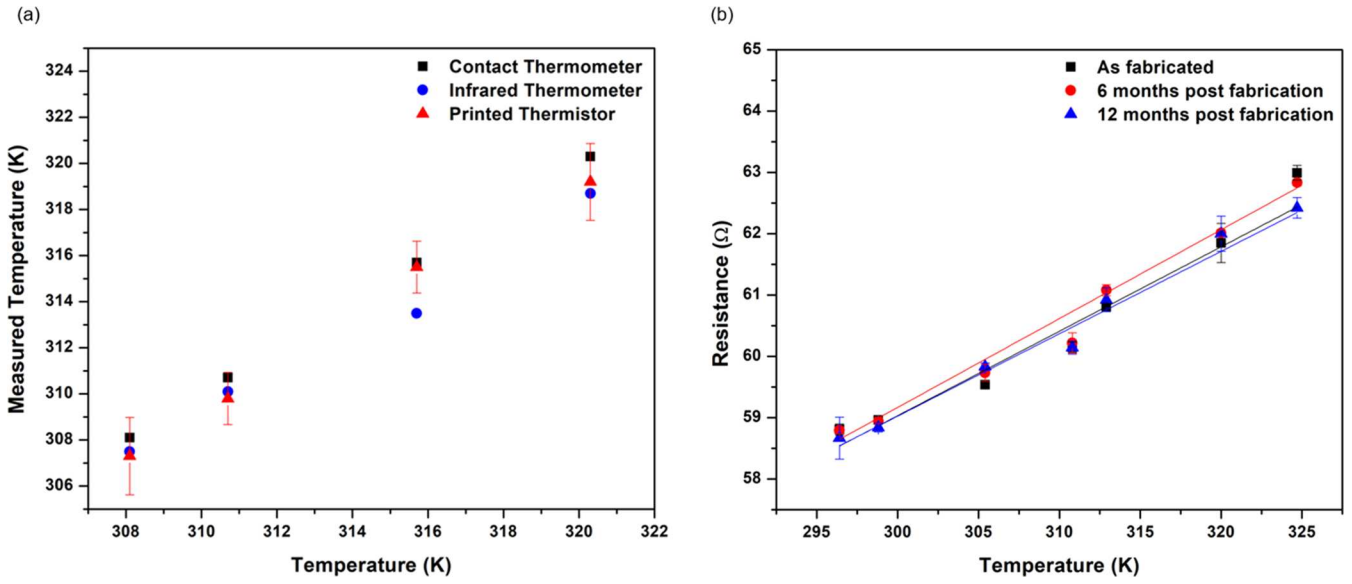

Figure 4. Thermistor performance evaluation. (a) Measured temperatures by a standard contact thermometer and a hand-held infrared thermometer compared to our printed thermistor. (b) Measured temperature-dependent resistance behavior of the thermistor printed at a power of 5.8 mW and a speed of 200 μm/s, as-fabricated compared to 6- and 12-months postfabrication.

This relationship between bubble morphology, printing parameters, and deposition characteristics plays a critical role in optimizing the printing process for the desired thermistors.[45]

Room-temperature (296 K) electrical characterization of the printed lines reveals a decreasing trend in measured resistance with printing laser power, as depicted in Figure 2c. A jump in the resistance occurs around the power range between 4.2 and 5.8 mW, corresponding to a shift from high resistance (represented in blue) to low resistance (represented in pink). The high resistance region and the low resistance region are expected to display NTC and PTC behavior, respectively. Within the presumed PTC region, the average thermal resistance decreases as laser power increases due to a higher deposition and subsequent enhancement of conducting behavior. As shown in Figure 2d, as the printing speed increases, the electrical conductance decreases. Low resistance is observed up to 800 μm/s, while high resistance is evident at 1000 and 1200 μm/s. Higher printing speeds lead to reduced Ag deposits, resulting in smaller grain structures. The higher resistivity values in our printed wires are attributed to the presence of narrower sidewalls and grain boundaries, contributing to electronic scattering and a rise in resistance.[24,53]

3.2. Thermistor Behavioral Characteristics. For PTC elements, the relationship between resistance and temperature can be approximated by a first-order equation

$$\Delta R = \alpha R(T)\Delta T \tag{1}$$

Here, α is the temperature coefficient of resistance and characterizes the sensitivity of resistance to the temperature, $R(T)$ is the resistance at a reference temperature T, ΔR is the change of resistance, and ΔT is the change of temperature.

The relationship between temperature and resistance for NTC elements is expressed by a modified Steinhart−Hart equation

$$\log R = \frac{\beta}{T} + \log r_{\infty} \tag{2}$$

where R and T are resistance and temperature, β is the thermal parameter, $r_{\infty} = R(T_0)e^{-\beta/T_0}$ is a modified Steinhart−Hart constant for a given material, and T_0 is a standard reference temperature (typically 298 K).

Based on the eqs 1 and 2, we consider linear resistive behavior between R and T to be indicative of a PTC thermistor and a linear relationship between log R and $\frac{1}{T}$ to be a NTC thermistor.

The measured thermal responses of the printed thermistors are illustrated in Figure 3. The thermistors printed at 2.6 and 4.2 mW laser power exhibit NTC behavior, displaying a linear relationship between log R and $\frac{1}{T}$ as plotted in Figure 3a. At powers of 5.8−9 mW, we observed PTC behavior with a linear increase in resistance with increase in temperature, shown in Figure 3b. Further, we observe PTC behavior for the printed thermistors at printing speeds from 200 to 800 μm/s, as represented in Figure 3c. We see a transition to NTC behavior at 1000 μm/s, as shown in Figure 3d. A more detailed discussion on the correlation of the deposition profiles and the electrical characterization with their corresponding electron microscopy images can be found in the Supporting Information file.

3.3. Temperature-Sensing Performance and Degradation. To assess the temperature-sensing performance of the printed thermistors, we performed a validation study using a standard infrared thermometer in a dry oven. Measured temperatures from the printed thermistors are within the error range of the contact thermometers, as shown in Figure 4a. The infrared thermometer displayed slightly different values compared to the contact thermometer, but within the range of error. Further, a characterization of the degradation behavior of the thermistors was conducted. The plotted temperatures were linearly fitted, resulting in the fitting equations of $0.138x + 17.727$ for the as-fabricated thermistors, $0.145x + 15.697$ after 6-months and $0.1344x + 18.714$ 12-months postfabrication, presented in Figure 4b. The calibration curve for the thermistors was observed to have undergone a slight shift

https://doi.org/10.1021/acs.jpcc.4c00598
J. Phys. Chem. C 2024, 128, 7316−7322

within the temperature range of operation; however, measured values remained in proximity to the original curve. This shift is potentially due to the degradation of the exposed silver electrodes, as the oxidation of silver in air is a well-known phenomenon. However, this can be eliminated with the appropriate circuit design and sealing, which is beyond the scope of this work.

CONCLUSIONS

We demonstrated versatile bubble printing of Ag thermistor arrays with tunable electrical behavior. By controlling the printing speed and bubble size, we tune the deposition profiles of the microscale thermistors and consequently their electrical characteristics. Both PTC and NTC thermistor arrays are achieved by simply tuning the laser power and printing speed. The printed thermistors exhibit a consistent performance in the sensing of surface temperatures even after 1 year of their fabrication. Our work demonstrates the feasibility of bridging the gap between high-throughput printing and submicron structuring of printed materials that allow a high tunability of the functions for their wider applicability.

ASSOCIATED CONTENT

Supporting Information

The Supporting Information is available free of charge at https://pubs.acs.org/doi/10.1021/acs.jpcc.4c00598.

Tilted scanning electron microscopy images of printed thermistors; discussion about electrical behavior and correlation to printing parameters (PDF)

AUTHOR INFORMATION

Corresponding Author

Yuebing Zheng − *Texas Materials Institute, The University of Texas at Austin, Austin, Texas 78712, United States; Walker Department of Mechanical Engineering, The University of Texas at Austin, Austin, Texas 78712, United States;* orcid.org/0000-0002-9168-9477; Email: zheng@austin.utexas.edu

Authors

Anand Swain − *Texas Materials Institute, The University of Texas at Austin, Austin, Texas 78712, United States*

Pavana Siddhartha Kollipara − *Walker Department of Mechanical Engineering, The University of Texas at Austin, Austin, Texas 78712, United States;* orcid.org/0000-0003-0166-6720

Complete contact information is available at: https://pubs.acs.org/10.1021/acs.jpcc.4c00598

Author Contributions

Y.Z., P.S.K., and A.S. conceived the idea and designed the experiments. A.S. carried out the printing of thermistors and performed measurements and data analysis. Y.Z. supervised the project. All authors were involved in discussing the results and writing the manuscript.

Funding

This work was funded by the National Science Foundation (NSF-PFI-2140985 and NSF-CMMI-1761743).

Notes

The authors declare no competing financial interest.

REFERENCES

(1) Ramanathan, K.; Danielsson, B. Principles and applications of thermal biosensors. *Biosens. Bioelectron.* **2001**, *16* (6), 417−423.

(2) Kühl, M. Optical microsensors for analysis of microbial communities. *Methods Enzymol.* **2005**, *397*, 166−199.

(3) Yu, L.; Wang, W.; Zhang, X.; Zheng, W. In *A review on leaf temperature sensor: Measurement methods and application*, Computer and Computing Technologies in Agriculture IX: 9th IFIP WG 5.14 International Conference, CCTA 2015, Beijing, China, September 27−30, 2015, Revised Selected Papers, Part I 9; Springer, 2016; pp 216−230.

(4) Lee, C.-Y.; Shen, C.-C.; Lee, S.-J.; Chiu, C.-W.; Lin, H.-T. Real-time microscopic monitoring of temperature and strain on the surface of magnesium hydrogen storage tank by high temperature resistant flexible integrated microsensor. *Int. J. Hydrogen Energy* **2022**, *47* (25), 12815−12821.

(5) Martínez-Cisneros, C. S.; Ibáñez-García, N.; Valdés, F.; Alonso, J. LTCC microflow analyzers with monolithic integration of thermal control. *Sens. Actuators, B* **2007**, *138* (1), 63−70.

(6) Wang, J.; Xue, D.; Li, X. Silicon monolithic microflow sensors: a review. *J. Micromech. Microeng.* **2021**, *31* (10), No. 104002.

(7) Colin, S. Gas microflows in the slip flow regime: a critical review on convective heat transfer. *J. Heat Transfer* **2012**, *134* (2), No. 020908.

(8) Aleksić, O. S.; Nikolić, P. M. Recent advances in NTC thick film thermistor properties and applications. *Facta universitatis-series: Electron. Energy* **2017**, *30* (3), 267−284.

(9) Key, D. J. Integration of thermal imaging with subsurface radiofrequency thermistor heating for the purpose of skin tightening and contour improvement: a retrospective review of clinical efficacy. *J. Drugs Dermatol.: JDD* **2014**, *13* (12), 1485−1489.

(10) Balčytis, A.; Ryu, M.; Juodkazis, S.; Morikawa, J. Micro-thermocouple on nano-membrane: thermometer for nanoscale measurements. *Sci. Rep.* **2018**, *8* (1), No. 6324.

(11) Lanzetta, F.; Gavignet, E.; Amrane, S.; Baucour, P. Micro-thermocouples sensors for velocity and temperature measurements in gas flow. In *Engineering Systems Design and Analysis*; American Society of Mechanical Engineers, 2012; Vol. *44854*, pp 231−240.

(12) Schena, E.; Tosi, D.; Saccomandi, P.; Lewis, E.; Kim, T. Fiber optic sensors for temperature monitoring during thermal treatments: An overview. *Sensors* **2016**, *16* (7), 1144.

(13) Yu, Q.; Zhou, X. Pressure sensor based on the fiber-optic extrinsic Fabry-Perot interferometer. *Photonic Sens.* **2011**, *1*, 72−83.

(14) Christofferson, J.; Maize, K.; Ezzahri, Y.; Shabani, J.; Wang, X.; Shakouri, A. Microscale and nanoscale thermal characterization techniques. *J. Electron. Packag.* **2008**, *130* (4), No. 041101.

(15) Kamat, R. K.; Naik, G. M. Thermistors−in search of new applications, manufacturers cultivate advanced NTC techniques. *Sens. Rev.* **2002**, *22* (4), 334−340.

(16) Hrovat, M.; Belavič, D.; Kita, J.; Cilenšek, J.; Golonka, L.; Dziedzic, A. Thick-film temperature sensors on alumina and LTCC substrates. *J. Eur. Ceram. Soc.* **2005**, *25* (15), 3443−3450.

(17) Bell, J. G.; Graule, T.; Stuer, M. Barium titanate-based thermistors: Past achievements, state of the art, and future perspectives. *Appl. Phys. Rev.* **2021**, *8* (3), No. 031318.

(18) Affleck, L.; Seaton, J.; Leach, C. Characterisation of the R−T response of BaTiO3 thermistors on three different length scales. *J. Eur. Ceram. Soc.* **2007**, *27* (12), 3439−3444.

(19) Apostol, I.; Helerea, E.; Oltean, I.; Matoi, A. In *Obtaining the high performance PTC thermistors based on barium titanate*, 2008 11th International Conference on Optimization of Electrical and Electronic Equipment; IEEE, 2008; pp 119−124.

(20) Heinen, B.; Waser, R. Influence of the thickness and area of NiCr/Ag electrodes on the characteristics of BaTiO3-ceramic based positive-temperature-coefficient thermistors. *J. Mater. Sci.* **1998**, *33*, 4603−4608.

(21) Smith, D. S.; Ghayoub, N.; Charissou, I.; Bellon, O.; Abélard, P.; Edwards, A. H. Transient thermal gradients in barium titanate

positive temperature coefficient (PTC) thermistors. *J. Am. Ceram. Soc.* **1998**, *81* (7), 1789−1796.
(22) Dewitte, C.; Elst, R.; Delannay, F. On the mechanism of delamination fracture of BaTiO3-based PTC thermistors. *J. Eur. Ceram. Soc.* **1994**, *14* (6), 481−492.
(23) Zhao, X.; Guo, J.; Wang, J.; Yan, Y. A Metal Nanoparticle Thermistor with the Beta Value of 10 000 K. *Small* **2023**, *19* (5), No. 2205136.
(24) Gall, D. The search for the most conductive metal for narrow interconnect lines. *J. Appl. Phys.* **2020**, *127* (5), No. 050901.
(25) Josell, D.; Brongersma, S. H.; Tőkei, Z. Size-dependent resistivity in nanoscale interconnects. *Annu. Rev. Mater. Res.* **2009**, *39*, 231−254.
(26) Bishara, H.; Lee, S.; Brink, T.; Ghidelli, M.; Dehm, G. Understanding grain boundary electrical resistivity in Cu: the effect of boundary structure. *ACS Nano* **2021**, *15* (10), 16607−16615.
(27) Liu, Y.; Zhu, K.; Hui, F.; Yuan, B.; Zhang, C.; Ma, Y.; Zhang, X.; Lanza, M. Inkjet Printing: A Cheap and Easy-to-Use Alternative to Wire Bonding for Academics. *Cryst. Res. Technol.* **2022**, *57* (3), No. 2100210.
(28) Komuro, N.; Takaki, S.; Suzuki, K.; Citterio, D. Inkjet printed (bio) chemical sensing devices. *Anal. Bioanal. Chem.* **2013**, *405*, 5785−5805.
(29) Bourhis, F. L.; Kerbrat, O.; Hascoet, J.-Y.; Mognol, P. Sustainable manufacturing: evaluation and modeling of environmental impacts in additive manufacturing. *Int. J. Adv. Manuf. Technol.* **2013**, *69*, 1927−1939.
(30) Zub, K.; Hoeppener, S.; Schubert, U. S. Inkjet printing and 3D printing strategies for biosensing, analytical, and diagnostic applications. *Adv. Mater.* **2022**, *34* (31), No. 2105015.
(31) Lin, Y.; Chen, J.; Tavakoli, M. M.; Gao, Y.; Zhu, Y.; Zhang, D.; Kam, M.; He, Z.; Fan, Z. Printable fabrication of a fully integrated and self-powered sensor system on plastic substrates. *Adv. Mater.* **2019**, *31* (5), No. 1804285.
(32) Virgilio, F.; Prasciolu, M.; Ugo, P.; Tormen, M. Development of electrochemical biosensors by e-beam lithography for medical diagnostics. *Microelectron. Eng.* **2013**, *111*, 320−324.
(33) Sun, L. L.; Leo, Y. S.; Zhou, X.; Ng, W.; Wong, T. I.; Deng, J. Localized surface plasmon resonance based point-of-care system for sepsis diagnosis. *Mater. Sci. Energy Technol.* **2020**, *3*, 274−281.
(34) Trautmann, A.; Roth, G.-L.; Nujiqi, B.; Walther, T.; Hellmann, R. Towards a versatile point-of-care system combining femtosecond laser generated microfluidic channels and direct laser written microneedle arrays. *Microsyst. Nanoeng.* **2019**, *5* (1), 6.
(35) Laurila, M.-M.; Khorramdel, B.; Mäntysalo, M. Combination of E-jet and inkjet printing for additive fabrication of multilayer high-density RDL of silicon interposer. *IEEE Trans. Electron Devices* **2017**, *64* (3), 1217−1224.
(36) Kim, K.; Kim, G.; Lee, B. R.; Ji, S.; Kim, S.-Y.; An, B. W.; Song, M. H.; Park, J.-U. High-resolution electrohydrodynamic jet printing of small-molecule organic light-emitting diodes. *Nanoscale* **2015**, *7* (32), 13410−13415.
(37) Arapov, K.; Abbel, R.; de With, G.; Friedrich, H. Inkjet printing of graphene. *Faraday Discuss.* **2014**, *173*, 323−336.
(38) Sun, J.; Kuang, M.; Song, Y. Control and application of "coffee ring" effect in inkjet printing. *Prog. Chem.* **2015**, *27* (8), 979.
(39) Wang, X.; Zhang, M.; Zhang, L.; Xu, J.; Xiao, X.; Zhang, X. Inkjet-printed flexible sensors: From function materials, manufacture process, and applications perspective. *Mater. Today Commun.* **2022**, *31*, No. 103263.
(40) Lohse, D. Fundamental fluid dynamics challenges in inkjet printing. *Annu. Rev. Fluid Mech.* **2022**, *54*, 349−382.
(41) Li, S.; Kosek, A.; Jahangir, M. N.; Malhotra, R.; Chang, C. H. Inkjet Printing of Perovskites for Breaking Performance−Temperature Tradeoffs in Fabric-Based Thermistors. *Adv. Funct. Mater.* **2021**, *31* (1), No. 2006273.
(42) Saeidi-Javash, M.; Du, Y.; Zeng, M.; Wyatt, B. C.; Zhang, B.; Kempf, N.; Anasori, B.; Zhang, Y. All-Printed MXene−Graphene Nanosheet-Based Bimodal Sensors for Simultaneous Strain and Temperature Sensing. *ACS Appl. Electron. Mater.* **2021**, *3* (5), 2341−2348.
(43) Schmidt, R.; Stiegelschmitt, A.; Roosen, A.; Brinkman, A. Screen printing of co-precipitated NiMn2O4+ δ for production of NTCR thermistors. *J. Eur. Ceram. Soc.* **2003**, *23* (10), 1549−1558.
(44) Turkani, V. S.; Maddipatla, D.; Narakathu, B. B.; Bazuin, B. J.; Atashbar, M. Z. A carbon nanotube based NTC thermistor using additive print manufacturing processes. *Sens. Actuators, A* **2018**, *279*, 1−9.
(45) Lin, L.; Peng, X.; Mao, Z.; Li, W.; Yogeesh, M. N.; Rajeeva, B. B.; Perillo, E. P.; Dunn, A. K.; Akinwande, D.; Zheng, Y. Bubble-pen lithography. *Nano Lett.* **2016**, *16* (1), 701−708.
(46) Bangalore Rajeeva, B.; Lin, L.; Perillo, E. P.; Peng, X.; Yu, W. W.; Dunn, A. K.; Zheng, Y. High-resolution bubble printing of quantum dots. *ACS Appl. Mater. Interfaces* **2017**, *9* (19), 16725−16733.
(47) Ghosh, S.; Ranjan, A. D.; Das, S.; Sen, R.; Roy, B.; Roy, S.; Banerjee, A. Directed self-assembly driven mesoscale lithography using laser-induced and manipulated microbubbles: complex architectures and diverse applications. *Nano Lett.* **2021**, *21* (1), 10−25.
(48) Tiwari, R., Jr; Maji, K.; Aji, A.; Ghosh, S.; Haldar, D.; Ghosh, N.; Banerjee, A. Directed self-assembly of a bio-inspired peptide into ring microstructures using micro-bubbles induced in thermo-optical tweezers. In *Optical Trapping and Optical Micromanipulation XVII*; SPIE, 2020; Vol. *11463*, pp 150−159.
(49) Rajeeva, B. B.; Kunal, P.; Kollipara, P. S.; Acharya, P. V.; Joe, M.; Ide, M. S.; Jarvis, K.; Liu, Y.; Bahadur, V.; Humphrey, S. M.; Zheng, Y. Accumulation-driven unified spatiotemporal synthesis and structuring of immiscible metallic nanoalloys. *Matter* **2019**, *1* (6), 1606−1617.
(50) Namura, K.; Sono, T.; Kumar, S.; Nakajima, K.; Suzuki, M. Thermochromic visualization of the heated region around a microbubble during Marangoni flow generation. *J. Nanophotonics* **2021**, *15* (1), 016007.
(51) Jones, S.; Andren, D.; Antosiewicz, T. J.; Stilgoe, A.; Rubinsztein-Dunlop, H.; Kall, M. Strong transient flows generated by thermoplasmonic bubble nucleation. *ACS Nano* **2020**, *14* (12), 17468−17475.
(52) Feteira, A. Negative temperature coefficient resistance (NTCR) ceramic thermistors: an industrial perspective. *J. Am. Ceram. Soc.* **2009**, *92* (5), 967−983.
(53) Wang, D. J.; Qiu, J.; Guo, Y.; Gui, Z.; Li, L. Grain boundary effects in NTC-PTC composite thermistor materials. *J. Mater. Res.* **1999**, *14* (1), 120−123.

https://doi.org/10.1021/acs.jpcc.4c00598
J. Phys. Chem. C 2024, 128, 7316−7322